

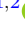







Toward XUV frequency comb spectroscopy of the 1S–2S transition in He⁺

Jorge Moreno¹ , Fabian Schmid¹ , Johannes Weitenberg^{1,2} , Savely G. Karshenboim^{1,3} ,
Theodor W. Hänsch^{1,3}, Thomas Udem^{1,3} , and Akira Ozawa^{1,a} 

¹ Max-Planck-Institut für Quantenoptik, Hans-Kopfermann-Straße 1, 85748 Garching, Germany

² Fraunhofer-Institut für Lasertechnik ILT, Steinbachstraße 15, 52074 Aachen, Germany

³ Fakultät für Physik, Ludwig-Maximilians-Universität München, Schellingstraße 4, 80799 Munich, Germany

Received 5 February 2023 / Accepted 31 March 2023 / Published online 24 April 2023
© The Author(s) 2023

Abstract. The energy levels of hydrogen-like atoms and ions are accurately described by bound-state quantum electrodynamics (QED). He⁺ ions have a doubly charged nucleus, which enhances the higher-order QED contributions and makes them interesting for precise tests of QED. Systematic effects that currently dominate the uncertainty in hydrogen spectroscopy, such as the second-order Doppler shift and time-of-flight broadening, are largely suppressed by performing spectroscopy on trapped and cooled He⁺ ions. Measuring a transition in He⁺ will extend the test of QED beyond the long-studied hydrogen. In this article, we describe our progress toward precision spectroscopy of the 1S–2S two-photon transition in He⁺. The transition can be excited by radiation at a wavelength of 60.8 nm generated by a high-power infrared frequency comb using high-order harmonic generation (HHG). The He⁺ ions are trapped in a Paul trap and sympathetically cooled with laser-cooled Be⁺ ions. Our recently developed signal detection scheme based on secular-scan spectrometry is capable of detecting He⁺ excitation with single-event sensitivity.

1 Introduction

Light hydrogen-like atoms and ions are the simplest bound systems, and their energy levels are accurately described by bound state quantum electrodynamics (QED) [1–5]. The theoretical expressions include the contributions of the electron self-energy and the vacuum polarization which go beyond the description by relativistic quantum mechanics using the Dirac equation. Theoretical predictions based on QED can be compared with spectroscopic measurements. Any discrepancy would reveal possible errors in the experiments and in the evaluation of the theoretical contributions or could point to new physics beyond the Standard Model. The measurement of the anomalous magnetic moment of the electron [6, 7] and the determination of the fine structure constant [8, 9] serve as precise tests of free-particle QED [10], which has been calculated to an impressive level of five-loop diagrams [11]. Meanwhile, the study of various transitions of different atomic and

ionic systems provides tests of bound-state QED that are complementary.

A precise test of bound-state QED requires a spectroscopic target that can be accurately measured. Since the 2S state is long-lived and the 1S–2S transition has a high quality factor, it is particularly interesting for high-precision spectroscopy. The frequency of the 1S–2S transition of atomic hydrogen has been measured with a fractional uncertainty of 4.5×10^{-15} , mainly limited by the second-order Doppler effect [12]. Combined with spectroscopic measurements of other transitions of hydrogen-like systems, the Rydberg constant and the nuclear charge radii can be determined. It was found that these constants extracted from different combinations of measurements do not agree with each other (the proton charge radius puzzle) [13–15]. The fine structure constant and the electron–nucleus mass ratio are other important parameters that enter the QED theory describing hydrogen-like systems. They are well known and introduce negligible uncertainties in the QED test [2, 8, 16, 17].

So far, the most accurate QED tests based on spectroscopy of two-body atomic systems have been performed only on hydrogen and deuterium. It is important to test whether QED accurately describes hydrogen-like systems with a nuclear charge Z greater than unity. The hydrogen-like He⁺ ion is an interesting spectroscopic target for this purpose. Higher-order QED corrections

Guest editors: Paolo Crivelli, Krzysztof Pachucki, Wim Ubachs, Thomas Udem, and Stefan Ulmer.

Precision Physics of Simple Atomic Systems.

^a e-mail: akira.ozawa@mpq.mpg.de (corresponding author)

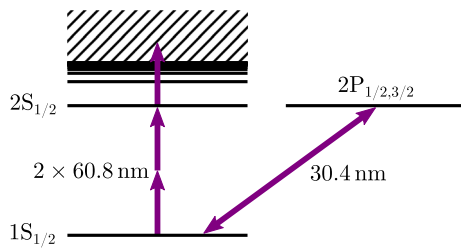


Fig. 1 Level scheme of ${}^4\text{He}^+$. We plan to excite the $1S$ – $2S$ two-photon transition using an XUV frequency comb at 60.8 nm . The $2S$ state can be ionized by radiation with a wavelength below 91.1 nm

scale with large exponents of the nuclear charge, making this measurement much more sensitive to these corrections compared to the hydrogen case. It could also provide additional insight into the proton charge radius puzzle. Due to their charge, He^+ ions can be held nearly motionless in the field-free environment of a Paul trap, providing ideal conditions for a high-precision measurement.

We are currently setting up an experiment to perform precise spectroscopy of the $1S$ – $2S$ transition in He^+ [18]. The main challenge of the experiment is that driving the transition requires coherent radiation at 60.8 nm (see Fig. 1). This is in the extreme ultraviolet (XUV) spectral region, where no continuous-wave laser source exists. The natural linewidth of the transition is narrow ($\Gamma = 2\pi \times 84 \text{ Hz}$) [19], and a narrow linewidth spectroscopy laser is required to drive it efficiently. We want to use two-photon direct frequency comb spectroscopy with a low-noise XUV frequency comb. The XUV comb is generated from a high-power infrared frequency comb using resonator enhanced high harmonic generation. The spectroscopic target will be a small number of He^+ ions trapped in a linear Paul trap and sympathetically cooled by co-trapped Be^+ ions. After successful excitation to the $2S$ state, a significant fraction of the He^+ ions are further ionized to He^{2+} that remain in the Paul trap. Sensitive charge-to-mass measurements using secular excitation will reveal the number of trapped He^{2+} ions and will serve as a single-event sensitive spectroscopy signal.

In this article, we describe our recent progress toward high-precision spectroscopy of the $1S$ – $2S$ transition in He^+ . In Sect. 2, we discuss the impact of the planned measurement on QED tests and the proton charge radius puzzle. In Sect. 3, we describe our setup to generate the frequency comb at 60.8 nm and the stabilization scheme to suppress its phase noise. The ion trap setup for storing the He^+ ions is described in Sect. 4, as well as our recent demonstration of the signal detection scheme. Before performing the $1S$ – $2S$ spectroscopy of He^+ , we plan to excite a two-photon transition in Be^+ ions which can be used for testing the alignment of our spectroscopy setup. This experiment is briefly discussed in Sect. 5.

2 Impact on QED

The precision of QED tests is limited partly by uncertainties in the theoretical expressions and its input parameters and partly by systematic and statistical uncertainties of the experiments. In this paper, the term “theory uncertainty” represents the uncertainty in the evaluation of the QED contributions, excluding the uncertainty due to the input parameters. A brief summary of the recent progress in the theory applied to hydrogen-like ${}^4\text{He}^+$ will be given here. For the frequency of the $1S$ – $2S$ transition in ${}^4\text{He}^+$, the corrections of order $\alpha^2(Z\alpha)^6 mc^2/h$ (and higher orders) due to the two-loop self-energy of the electron have the largest theoretical uncertainty. Recently, an updated evaluation of this contribution was reported with a reduced uncertainty of 32 kHz (3×10^{-12} relative to the transition frequency) [20–24]. The updated two-loop correction [22] is not yet included in the current CODATA2018 report [2] (see also [4]). Other important contributions to the uncertainty originate from the three-loop corrections and the radiative recoil effects. For ${}^4\text{He}^+$, they are estimated to be 9.5 and 12 kHz , respectively [22, 25]. For ${}^3\text{He}^+$ the radiative recoil corrections have an uncertainty of 16 kHz [22]. The evaluation of the relativistic recoil corrections was improved recently [26], and the result now has a negligible uncertainty compared to the uncertainty of the two-loop contributions. The calculations of the leading four-loop corrections were completed [27–30], and their uncertainties are insignificant at the current level of precision. In total, the theory uncertainty of the $1S$ – $2S$ transition frequency of ${}^4\text{He}^+$ is estimated to be $\sim 36 \text{ kHz}$ (4×10^{-12}).

The recent measurement of the Lamb shift of muonic ${}^4\text{He}^+$ allows a precise determination of the charge radius of the ${}^4\text{He}^+$ nucleus (α -particle) [31]. The result is in agreement with the elastic electron scattering of ${}^4\text{He}$ [32] and has about a five times smaller uncertainty, corresponding to 60 kHz with respect to the $1S$ – $2S$ transition frequency of ${}^4\text{He}^+$ (6×10^{-12}) [31, 33].

Higher-order contributions of the finite nuclear size effects for electronic ${}^3,4\text{He}^+$, such as the two- and three-photon exchange contributions, are less well known, but are not expected to significantly affect the uncertainty. For example, the nuclear polarizability contribution was evaluated with a 3 kHz uncertainty for ${}^4\text{He}^+$ [34]. The uncertainty of the nuclear charge radius obtained from muonic ${}^4\text{He}^+$ spectroscopy is dominated by the two-photon exchange contributions including the effects of nuclear polarizability [31]. A possible correlation of nuclear structure uncertainties in the muonic and electronic systems with the same nucleus should be considered when including higher-order contributions in future QED tests.

The charge radius of the ${}^4\text{He}^+$ nucleus currently introduces a larger uncertainty (60 kHz) than the theory uncertainty (36 kHz) [31, 33]. Therefore, a measurement of the ${}^4\text{He}^+$ $1S$ – $2S$ transition frequency with an uncertainty of smaller than 60 kHz (6×10^{-12}) would improve the determination of the charge radius, assum-

ing that QED is correct. Moreover, it could be used to determine the two-photon exchange contribution to the muonic ${}^4\text{He}^+$ energy levels which would serve as an important test of nuclear polarizability theory. Measuring more than one transition in ${}^4\text{He}^+$ determines the Rydberg constant and the charge radius and would allow an independent QED test without relying on hydrogen and deuterium results. The proton charge radius puzzle corresponds to a discrepancy of about 4×10^{-11} for the Rydberg constant. A measurement of the 1S–2S transition frequency of ${}^4\text{He}^+$ with an uncertainty of less than 4×10^{-11} (~ 400 kHz) would determine the Rydberg constant at this level and thus could help to solve the puzzle.

In the future, it would also be interesting to perform spectroscopy on the ${}^3\text{He}^+$ isotope. In principle, this can be done with the same experimental apparatus and spectroscopy scheme used for ${}^4\text{He}^+$. The two-loop and three-loop contributions are common to ${}^3,4\text{He}^+$ and will cancel out completely when the results are combined. The radiative recoil corrections and their uncertainties are strongly suppressed. Therefore, the measurement will determine the charge radius difference $\Delta r^2 = r({}^3\text{He})^2 - r({}^4\text{He})^2$ with a smaller uncertainty than the radii themselves. The result can be compared to isotope shift measurements of neutral ${}^3,4\text{He}$, where the problematic high-order three-body QED contributions are largely cancelled out [35–41]. Measurements of different transitions starting from the metastable 2^3S state of neutral ${}^3,4\text{He}$ show statistically significant inconsistencies [35, 36]. The measurements on the ${}^3,4\text{He}^+$ isotopes may provide new insight into this problem. The squared radius difference can also be obtained by measuring the isotope shift in muonic ${}^3,4\text{He}^+$. However, the uncertainty is dominated by the two-photon exchange contributions. Since these are isotope-dependent, no significant cancellation takes place. The uncertainties in the QED theory are partially correlated for hydrogen, deuterium, and ${}^3,4\text{He}^+$. The results of spectroscopic measurements on these species can be analyzed together by a global fit to the theory that takes advantage of the known correlations between the uncertainties.

3 Laser setup

Our setup for the generation of a 60.8-nm XUV frequency comb consists of the following components (see Fig. 2). We start with a 1030-nm Yb:KYW Kerr-lens mode-locked oscillator that emits < 100 fs pulses at a 40 MHz repetition frequency, with an average power of 10 mW. The laser is pumped by a single-mode-fiber coupled diode-laser at 981 nm with an average power of 500 mW. We use a two-stage preamplifier and a main amplifier to increase the average power for subsequent frequency conversion to the XUV. The two-stage Yb:LuAG solid state preamplifier produces a power of 2.7 W. Its output is used to seed a high-power Yb:YAG Innoslab amplifier [42]. That brings the average power up to 270 W after a Faraday isolator and a spatial fil-

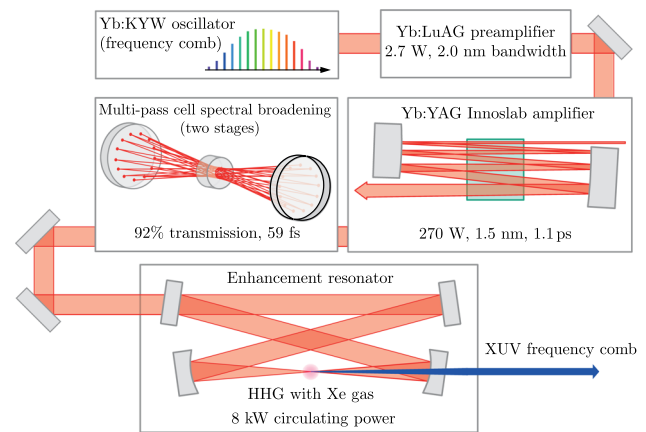


Fig. 2 Simplified schematic of the XUV comb setup. The seed laser is a Yb:KYW Kerr-lens mode-locked oscillator. A two-stage preamplifier and the Innoslab amplifier [42], together with the multi-pass cells for pulse compression [43], provide high-power ultrashort pulses. The XUV comb is produced via resonator-enhanced high-harmonic generation (HHG)

ter to improve the beam quality. The gain bandwidth of the Yb:YAG crystal together with the small seed bandwidth of 2 nm limits the amplified bandwidth to 1.5 nm and sets the pulse duration to 1.1 ps with a center wavelength of 1030 nm. The amplifier is followed by a nonlinear pulse compression, i.e., nonlinear spectral broadening and subsequent chirp removal, in order to cover a larger spectrum that includes 1033 nm, the 17th subharmonic of the 1 S–2 S two-photon transition frequency at 60.8 nm. In addition, shorter pulses allow for a higher conversion efficiency. We employ a multi-pass-cell spectral broadening (MPCSB) scheme which is suitable for a pulse energy range of a few μJ and for high average power [43, 44]. Two stages are used for spectral broadening from a spectral width of 1.5 nm to a spectrum that extends beyond 1010 nm and 1060 nm (see Fig. 3). Each stage consists of a multi-pass cell (MPC) with two 2''-diameter concave mirrors and an AR-coated fused-silica plate placed in the center as the nonlinear element. The MPC mirrors have a dispersive coating in order to compensate the material dispersion of the element. The first stage uses a 20-mm element with 45 passes, while the second stage uses a 13-mm element with 21 passes. After spectral broadening, the spectral chirp is removed using a set of dispersive mirrors and a tunable transmission-grating pair. The temporal pulse duration after the chirp removal is 59 fs, characterized by frequency-resolved optical gating (FROG). The total throughput of the pulse compression setup including two MPCs and chirp removal is $\sim 92\%$, and nearly 250 W can be used for frequency conversion to the XUV. The beam quality after the multi-pass cells is measured to be $M^2 = 1.1 \times 1.05$.

The XUV frequency comb covering the two-photon transition wavelength at 60.8 nm is synthesized by resonator-enhanced high-harmonic generation (HHG) of our infrared frequency comb close to 1033 nm [45–

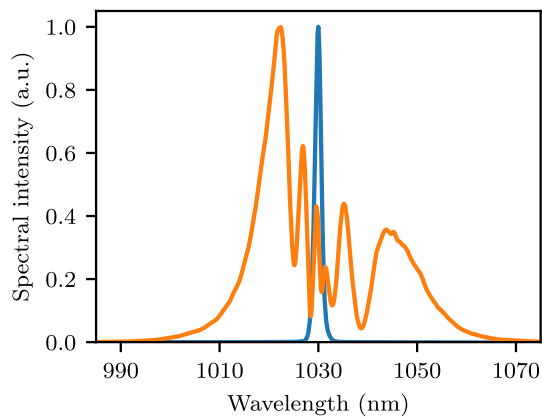


Fig. 3 Spectra of our Yb-based infrared laser measured before and after the multi-pass cells for spectral broadening and pulse compression (blue and orange traces, respectively). The broadened spectrum is obtained at ~ 240 W of power measured after the compression, and has significant spectral intensity from 1010 to 1060 nm. The pulse duration after chirp removal is 59 fs

48]. HHG is a strongly nonlinear process that coherently generates odd-order harmonics from a high-intensity driving field. The process is demonstrated to preserve the frequency comb structure [49]. The phase noise of the driving laser is multiplied in the HHG process: the rms phase noise of the q th harmonic is given by $q\phi_{\text{rms}}$, where ϕ_{rms} is the rms phase noise at the fundamental wavelength. The fractional power contained in the carrier of the q th harmonic radiation is $\exp(-q^2\phi_{\text{rms}}^2)$. Therefore, the phase noise of the fundamental wavelength ϕ_{rms} has to be kept sufficiently low to avoid a significant reduction of the carrier power or complete disappearance of the carrier (carrier collapse). For the purpose of two-photon direct comb spectroscopy, it is sufficient to stabilize one of the comb modes as shown in Fig. 4. In this case, the residual phase noise is symmetric around the frequency of the stabilized mode and cancels out in a two-photon excitation. We achieve this by tightly locking one infrared comb mode to a continuous wave (CW) reference laser at 1033 nm, corresponding to 1/17 of the 1 S–2 S two-photon transition frequency. The reference CW laser is stabilized to an ultra-stable reference cavity [50]. In addition, the phase noise introduced by path length fluctuations along the setup is measured by heterodyne beat detection with the same reference laser, right before the enhancement resonator for HHG. An acousto-optic modulator (AOM) is placed after the preamplifier to precompensate for these fluctuations. The phase noise characterization of our reference laser is described in [50]. In addition, we have performed an in-loop measurement of the residual phase noise between the frequency comb mode and the reference laser. The enhancement resonator filters out phase noise with Fourier frequencies above its linewidth [51]. By numerically filtering the measured noise spectra with the expected noise transfer function, we estimate that the light circulating in the enhancement resonator has

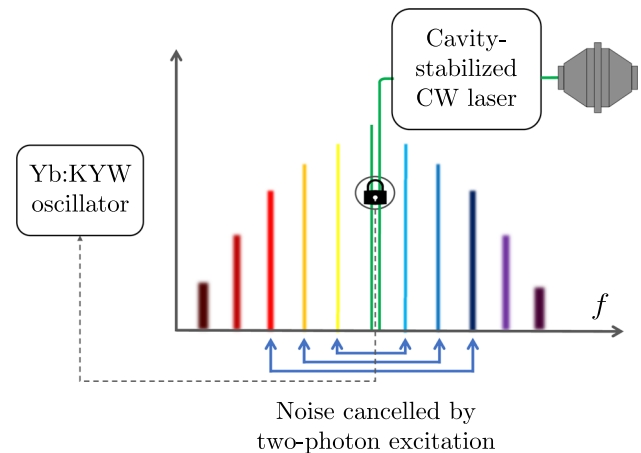


Fig. 4 Frequency comb stabilization scheme. One of the comb modes is stabilized to a reference CW laser at 1033 nm. The reference CW laser is stabilized to an ultra-stable reference cavity. The residual phase noise of the infrared frequency comb is symmetric around the stabilized mode. When pairs of symmetrically detuned modes (indicated by blue arrows) participate in the two-photon excitation, their noise contributions cancel out

an integrated phase noise of around 14 mrad. This corresponds to 80% of the power remaining in the carrier at the 34th harmonic. The path length of the XUV beamline between the HHG and the ions (see below) is not actively stabilized. Length fluctuations due to vibrations add phase noise and have to be minimized. We use vibration dampers on the turbomolecular pumps of the setup and plan to interferometrically measure the mirror vibrations using auxiliary laser beams.

A bow-tie resonator is used for the resonator enhanced HHG. The resonator length is stabilized by locking it to the reference CW laser rather than to the infrared comb directly. In this way, we avoid modulation sidebands on the frequency comb that are required to generate the Pound–Drever–Hall error signal [52]. Similar to the phase noise, these sidebands would reduce the carrier power. The dispersion from the highly reflective resonator mirrors is small enough to support the spectral bandwidth obtained from the MPC spectral-broadening setup. High-harmonics are generated at the tight focus of the enhancement resonator where a Xe gas jet acts as a nonlinear medium. The focal radius is $w_0 = 43 \mu\text{m}$. The generated XUV radiation is extracted from the resonator by using a HR mirror with a slit that is structured into the substrate, serving as the output coupler [53]. To avoid high losses in the infrared field due to the slit, the resonator is set in a *non-collinear configuration* [54] (see Fig. 5). In this configuration, the beams in the collimated arm of the resonator are contained in two distinct vertically offset planes, and the beam has to pass each mirror twice to complete a round trip. The beams in the focused arm have an intersection at the focus of the resonator. The total round trip length of the resonator is set to be 15 m, which corresponds to a free spectral range of 20 MHz. When

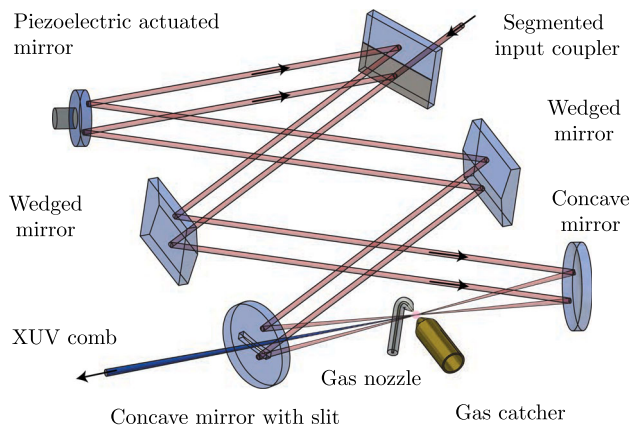


Fig. 5 A simplified schematic of the enhancement resonator for HHG. The resonator is operated in a non-collinear configuration. Two pulses are circulating simultaneously in the cavity and are spatially and temporally overlapped at the focus of the resonator, where harmonics are generated using a Xe gas jet as a nonlinear medium. The two wedge mirrors ensure that the two beams are parallel and the beam path is closed to complete a round trip. The generated harmonics exit the resonator through the slit in the output coupler. Additional folding mirrors (not shown) are used to fit the resonator into our vacuum system

seeded by the comb with 40 MHz mode-spacing, two pulses are simultaneously circulating in the resonator. These two pulses temporally and spatially overlap at the focus of the resonator where high harmonics are generated. A circulating power (adding the two circulating pulses) of up to 8 kW has been achieved at 120 W of impinging power. Currently, the enhanced power is limited by plasma effects [55]. The power loss per round-trip is estimated to be $< 0.2\%$ excluding the transmission at the input coupler. The HHG radiation propagates along the bisector of the two intersecting infrared beams. While the infrared beams avoid the slit in the output coupler, which is located at the bisector, the XUV pulses pass through it and exit the resonator with high efficiency.

A non-collinear configuration could be achieved with two enhancement resonators with intersecting beams [47] or with one resonator of twice the length and two circulating pulses [56] arranged to intersect in the focus. These proposals have not been demonstrated for HHG as they are difficult to align. Zhang et al. demonstrated HHG with a non-collinear resonator where two circulating pulses use different focusing mirrors but share the other resonator mirrors [54]. This still requires alignment of the focus position and timing of the pulses. In our resonator, the two beams share all resonator mirrors such that they are intrinsically synchronized and aligned [57]. This is possible by employing wedged mirrors in the resonator which imprint a different angle on the beams reflected from the two segments of the mirror. Moreover, we need the wedged mirrors to tune the phase delay between the two pulses by shifting them vertically (in Fig. 5). In our implementation we use a

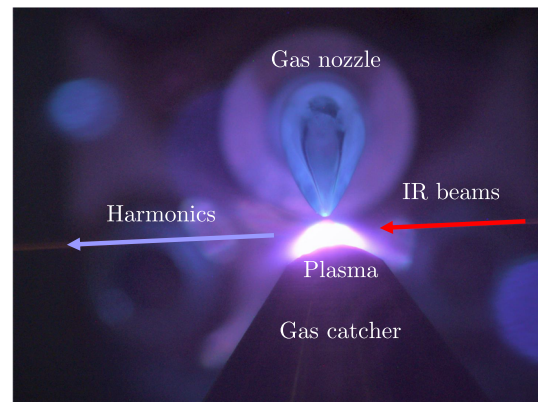


Fig. 6 An image of the resonator focus where high harmonics are generated in a Xe gas jet (top view). Optical emission from the plasma can be observed with the bare eye. A gas catcher is placed very close to the nozzle to reduce the background pressure

total of 16 mirrors, ten of which are 1" plane mirrors, one is a 1/2" piezo-actuated mirror as a fast actuator to stabilize the resonator length, one is the input coupler, two are wedged mirrors and two are focusing mirrors. These focusing mirrors have radii of curvature of 300 mm and 500 mm. The 300-mm mirror, placed behind the focus, has an open slit of 0.3 mm width and acts as the output coupler. The slit was structured via Inverse Laser Drilling [53]. The wedged mirrors have reflecting surfaces that are vertically tilted by $\pm 270 \mu\text{rad}$. Finally, the input coupler is segmented (88% transmission) and its upper half is highly reflective. The typical beam separation at the output coupler is 6.7 mm, and the beam radius is $w = 1.2 \text{ mm}$. The whole setup is placed in a vacuum chamber at a few times 10^{-3} mbar of pressure to avoid absorption of the XUV radiation by air. A gas catcher is placed opposite to the fused-silica gas nozzle (100 μm opening diameter) and is pumped by an independent roughing pump to efficiently capture the Xe gas (Fig. 6). The background pressure is currently limited by the gas flow from the nozzle and the pumping speed of the turbomolecular pumps installed on the housing. Two resonator mirrors are mounted in PZT actuated kinematic mounts such that the alignment of the resonator can be fine-tuned to compensate for misalignment due to thermal effects (not shown in Fig. 5). At the moment, the system can be operated continuously for more than one hour.

For characterization of the generated harmonics, a toroidal XUV grating with a known diffraction efficiency angularly separates the spectral components. The different harmonic orders are detected on a fluorescence plate (Scintillating Screen P43, Proxi Vision). A movable XUV sensitive photodiode (AXUV20HS1, Opto Diode) is installed next to the fluorescence plate and allows the determination of the generated power at different harmonic orders. As a preliminary result,

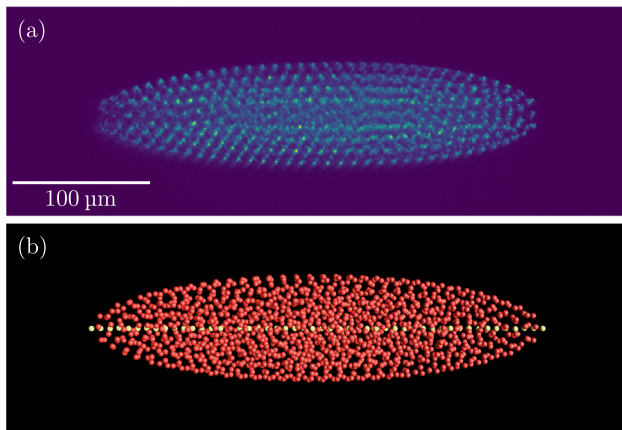


Fig. 7 Mixed Be^+/He^+ ion crystal. **a** Recorded fluorescence image showing laser cooled Be^+ ions. The sympathetically cooled He^+ ions experience stronger radial confinement and form a dark “core” in the center of the crystal. **b** Ion crystal structure obtained by a molecular dynamics simulation [59]. The simulation contains 1450 Be^+ ions (red spheres) and 50 He^+ ions (yellow spheres)

$\sim 10 \mu\text{W}$ per harmonic order are outcoupled from the resonator at wavelengths around 60.8 nm.

4 Ion trap setup

The spectroscopy target is a small number of He^+ ions that are held in an ion trap.

While He^+ ions can be easily loaded into an ion trap, the extremely short transition wavelengths preclude direct laser cooling with currently available laser sources (see Fig. 1). Instead, we mix the He^+ ions with co-trapped laser-cooled Be^+ ions. Due to the strong Coulomb interaction between the ions, the He^+ ions are sympathetically cooled. When the ions reach a sufficiently low temperature (typically a few tens of mK), they crystallize into a regular two-component ion crystal [58] (see Fig. 7).

We hold the ions in a linear Paul trap whose geometry is shown in Fig. 8. It consists of four “blade” electrodes for radial confinement and a pair of “endcap” electrodes for axial confinement. The blade electrodes have axial lengths of 3.00 mm, and their surfaces are located 0.45 mm from the trap axis. The trap drive at 66.05 MHz with an amplitude of around 120 V is generated with a helical radio frequency (RF) resonator [60]. It is applied to one diagonal pair of blade electrodes, while the other pair is held at DC voltages. A static voltage of 400 V is applied to the endcaps. The resulting secular frequencies for Be^+ are 1.6 MHz in the radial direction and 645 kHz in the axial direction. An additional compensation electrode is located between two of the blade electrodes. By adjusting the voltages of the DC electrodes and the compensation electrode, unwanted electric fields in the trap center can be compensated.

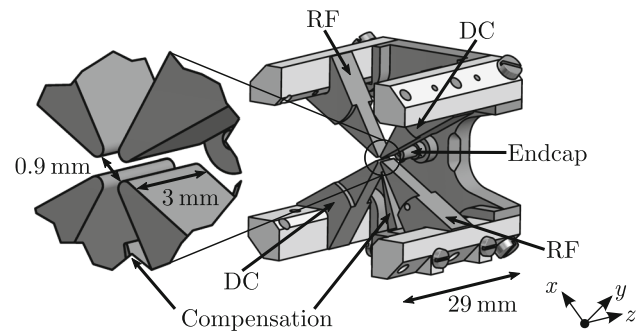


Fig. 8 Geometry of the ion trap. The trap axis is in the z -direction. Radial confinement is generated by applying a radio frequency to the RF electrodes. Two endcap electrodes are used for axial confinement. For clarity, only one of the endcaps is shown. Holes are drilled through the endcaps in order to allow for optical access along the trap axis. Static voltages can be applied to the compensation electrode and the DC electrodes in order to compensate for field asymmetries due to stray electric fields and electrode misalignment

For loading Be^+ ions into the trap, a beam of Be atoms is produced in an oven and is sent through the trapping region. There the atoms are resonantly ionized by a 235-nm laser beam [61]. The vacuum chamber housing the trap is equipped with a motorized leak valve that allows controlled introduction of gases. For loading He^+ ions, we fill the chamber with around 5×10^{-10} mbar of He. The atoms are then ionized inside the trapping region by an electron beam produced by a home-built electron gun.

The Be^+ ions are laser cooled by driving the $2s \ ^2S_{1/2} (F = 2) \rightarrow 2p \ ^2P_{3/2} (F = 3)$ cycling transition which has a wavelength of 313 nm and a natural linewidth of $\Gamma = 2\pi \times 18$ MHz [62]. The cooling laser light is generated as follows. First, light at 626 nm is produced by sum-frequency generation of the outputs of two CW fiber lasers at 1550 nm and 1051 nm in a periodically poled lithium niobate crystal. The light is then frequency doubled in a β -barium borate crystal in a resonant enhancement cavity [63]. The cooling laser is frequency stabilized by phase-locking the 626-nm light to one mode of a self-referenced optical frequency comb (Menlo Systems FC1500-250-ULN). In order to prevent pumping the ions into the $2s \ ^2S_{1/2} (F = 1)$ dark state, the transition is driven with circularly polarized light. In addition, a resonant electro-optic phase modulator (QUBIG PM-Be+_1.3P3) is used to generate 1.25 GHz sidebands on the cooling light which matches the ground-state hyperfine splitting in Be^+ [64, 65]. The lower sideband is therefore in resonance with the $2s \ ^2S_{1/2} (F = 1) \rightarrow 2p \ ^2P_{3/2} (F = 2)$ transition and acts as a repumper.

During operation of the XUV comb, the gas load from the Xe beam increases the pressure in the vacuum chamber containing the HHG enhancement resonator to a few times 10^{-3} mbar. At the same time, we want to keep the background pressure in the ion trap below 10^{-10} mbar to minimize ion loss due to collisions with

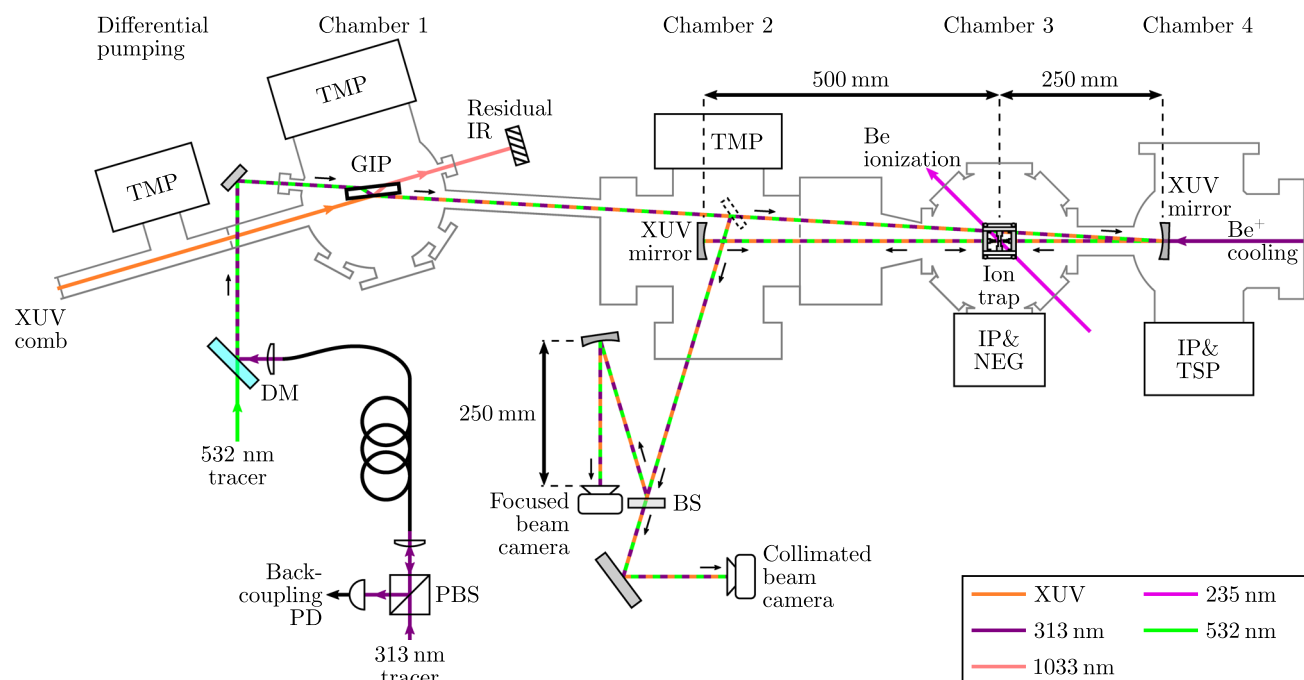


Fig. 9 Overview of the differentially pumped XUV beamline (not to scale). The grazing incidence plate (GIP) steers the radiation from the XUV frequency comb setup and splits off residual infrared light. It is also used for overlapping the XUV frequency comb with tracer beams. The 313-nm tracer is delivered via a UV resistant single-mode fiber. An insertable redirection mirror (dashed) can send light out of the vacuum chamber for adjusting the relative alignment of the XUV comb and the tracers. The beam is focused onto the ions by a concave XUV mirror (500 mm radius of curvature). A second identical mirror is used as a retroreflector. TMP, turbomolecular pump; IP, ion pump; NEG, non-evaporable getter; TSP, titanium sublimation pump; BS, beam splitter; PBS, polarizing beam splitter; DM, dichroic mirror

gas atoms or molecules. One possibility would be to separate the different regions with a thin aluminum foil (hundreds of nm thick) which has some transparency in the XUV and would also provide spectral filtering [18]. However, the extreme fragility of such foils makes them difficult to use as windows, and the large transmission losses would reduce the achievable signal rate. Instead, we have set up a differentially pumped vacuum beamline for delivering the radiation from the XUV frequency comb setup to the ion trap (see Fig. 9).

The first stage is a differential pumping section. In order to minimize the amount of gas flowing through, it is connected to the HHG enhancement resonator chamber with a 1.8-mm-diameter hole and to the following vacuum chamber with a 3.2-mm-diameter hole. Turbomolecular pumps are used to evacuate the differential pumping section and the subsequent two vacuum chambers of the beamline. Chambers 3 and 4 form the ultra-high vacuum section and are evacuated by ion pumps, a non-evaporable getter pump, and a titanium sublimation pump. A base pressure of around 3×10^{-11} mbar is reached in chamber 3 which houses the ion trap. No significant pressure increase is observed in chambers 1 to 4 when the Xe jet is operated at its current maximum backing pressure of 3 bar. This indicates that the differential pumping setup could handle significantly larger gas loads. In the future, this may allow operating the HHG with a He/Xe gas mixture which has been

shown to reduce the detrimental buildup of steady-state plasma in a resonator-enhanced HHG source [66].

The radiation that is coupled out from the HHG enhancement resonator can contain up to a few W of residual infrared light at the fundamental wavelength (centered around 1033 nm). This light could lead to a significant AC Stark shift of the 1S–2S transition and thermal damage in the subsequent optical components. The infrared light is therefore attenuated to $\sim 2.5\%$ by using a grazing incidence plate which is anti-reflection coated for the infrared wavelength. Since the plate is arranged at a very large angle of incidence (80° against the surface normal), we expect a reflectivity of around 70% at 60.8 nm from the top SiO_2 layer of the anti-reflection coating [67]. The plate is mounted in a motorized mirror mount and can be used for steering the beam through the setup. It is partially transparent for visible and ultraviolet light and can be used for overlapping the XUV comb with tracer beams. The first tracer has a wavelength of 532 nm and is used to make the beam alignment visible through the windows of the vacuum chambers. The second tracer is derived from the Be^+ cooling laser at 313 nm. This light makes the Be^+ ions fluoresce and can be used for fine tuning the alignment onto the ions.

The tracers have to be carefully overlapped with the XUV comb. For this purpose, a metallic broadband redirection mirror can be inserted into the beam path

using a mechanical vacuum feedthrough (dashed mirror in Fig. 9). The mirror sends the light out of the vacuum chamber through a window. Besides the tracer beams, the fundamental (1033 nm), 3rd harmonic (344 nm), and 5th harmonic (207 nm) contained in the XUV comb can pass through the fused silica vacuum window. The light is then split into two paths by a wedged beam splitter. The reflection is focused onto a camera using a concave metallic broadband mirror with 500 mm radius of curvature. This geometry matches the beam path that focuses the radiation onto the trapped ions (see below). The transmitted light is sent onto a second camera without focusing optics. Overlapping the spot positions in the images from the first camera ensures that the beams meet at the focus, but does not yet fix their relative angles. This is achieved by also overlapping the spots at the second camera.

Without the redirection mirror inserted, the beam passes through chambers 2 and 3 and encounters the first concave XUV mirror which is located in chamber 4. The mirror has a radius of curvature of 500 mm and is coated with a custom multi-layer coating (optiX fab GmbH) which achieves a measured reflectivity of 33.4% at 60.8 nm. The mirror focuses the radiation into the ion trap.

In principle, the 1S–2S transition in He^+ can be excited using a single laser beam. However, the small ion mass and the large photon momentum lead to a recoil shift of 54 MHz for $^4\text{He}^+$. This exceeds the achievable secular frequencies in our ion trap by an order of magnitude such that the Lamb–Dicke regime cannot be reached. The absorption spectrum would therefore be strongly modulated and would consist of a large number of motional sidebands [18]. This would significantly reduce the excitation rate. Furthermore, it could be challenging to determine the location of the carrier which is required for accurate spectroscopy. We therefore strongly suppress these motional effects by exciting the transition in an anti-collinear geometry using two counter-propagating laser beams. This is achieved by placing a second identical XUV mirror 500 mm behind the ion trap which reflects the beam back onto itself. The XUV mirrors are mounted in motorized mirror mounts which are placed on motorized linear stages for focus adjustment. The light for the 313-nm tracer beam is delivered to the setup using a UV resistant single-mode optical fiber [68]. When the second XUV mirror is adjusted correctly, the tracer beam is sent back through the setup, passes through the grazing incidence plate again, and is coupled back into the fiber. This back-coupled light is monitored using a polarizing beam splitter and a photodiode which are placed in front of the fiber. The signal from this photodiode is used to precisely adjust the alignment of the second XUV mirror.

Anti-collinear two-photon excitation requires that the excitation pulses collide at the ion position. At our repetition rate of 40 MHz, this would require placing the back-reflection mirror 3.75 m away from the ion trap, which requires an impractical size of the vacuum chambers. Instead, in our setup a Mach–Zehnder inter-

ferometer is inserted into the infrared frequency comb laser beam between the first and second preamplifier stage. This turns the frequency comb pulses into pulse pairs that are spaced by the path length difference of 1 m. Since the back-reflection mirror is placed 0.5 m behind the ion trap, the first and the second pulses of each pulse pair collide at the position of the ions. Note that during frequency conversion into the XUV, the pulses ionize Xe atoms in the gas jet and the two pulses may find the jet in different states. However, each pulse train (separated by $1/f_{\text{rep}}$) interacts with the gas jet under the same condition and we do not expect distortion of the comb structure.

Off-axis ions in a three-dimensional ion crystal experience radial micromotion. It is advantageous to align the cooling laser beam along the trap axis since this minimizes the influence of micromotion sidebands. In our setup direct optical access along the trap axis is blocked by the XUV mirrors. However, the mirrors transmit around 7% at 313 nm such that the cooling beam can be sent through the first XUV mirror. The light is focused by an $f = 500$ -mm lens which results in a spot size of $2w_0 \approx 180 \mu\text{m}$ in the center of the ion trap.

The spectroscopy experiment requires a scheme for detecting that the 1S–2S transition in the He^+ ions is being excited. We plan to employ state-dependent photoionization as follows. After successful excitation to the 2S state, He^+ ions can be ionized to He^{2+} by absorbing another photon with a wavelength below 91.1 nm. In our setup, the 13th and higher harmonic orders contained in the XUV comb can contribute to the ionization. The generated He^{2+} ions remain trapped and can serve as a sensitive and background-free signal for the spectroscopy experiment. Since both He^+ and He^{2+} are non-fluorescing (“dark”) ions, it is difficult to visually distinguish them in the fluorescence image of the ion crystal (Fig. 7a). We have recently demonstrated a method for tracking the number of dark ions embedded in an ion crystal in real time with single-particle sensitivity [59]. This is achieved by exciting the secular motional resonances of the dark ions by applying an oscillating electric field. The motional excitation heats the ions which changes the amount of fluorescence the coolant ions emit. Under suitable experimental conditions, discrete steps can be observed in the fluorescence signal when the number of dark ions changes. By counting the number of steps, the number of dark ions of each species can be identified unambiguously. In our previous publication [59], we demonstrated the scheme by detecting H_2^+ and H_3^+ ions embedded in a Be^+ ion crystal.

In order to test the detection scheme for the spectroscopy, we load a mixed Be^+/He^+ ion crystal similar to the one shown in Fig. 7. The electron beam used in the He^+ loading process also ionizes H_2 molecules from the residual gas in the vacuum chamber such that a few H_2^+ ions become embedded in the ion crystal. Since H_2^+ has the same charge-to-mass ratio as He^{2+} , this allows us to test the sensitivity of detecting He^{2+} . We excite

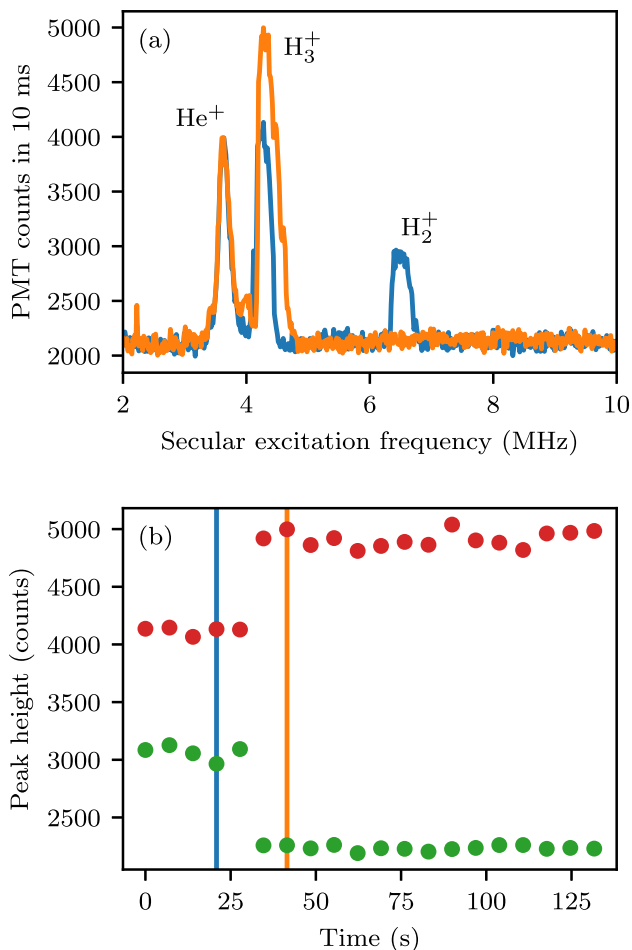


Fig. 10 **a** Secular spectra recorded with a photomultiplier tube (PMT) showing He⁺, H₃⁺, and H₂⁺ ions embedded in a Be⁺ ion crystal. The orange trace was recorded 21 s after the blue trace. In the meantime, the only present H₂⁺ ion has reacted to H₃⁺. **b** Time evolution of the H₂⁺ (green) and H₃⁺ (red) resonance peak heights. The data points corresponding to the two traces in (a) are indicated by the vertical lines

the radial secular motion of the ions by applying an oscillating voltage to the compensation electrode. The frequency is swept from 2 to 10 MHz in 500 steps, and at each step the fluorescence emitted by the Be⁺ ions is measured for 10 ms with a photomultiplier tube.

Figure 10a shows typical resulting secular spectra. The single-particle radial secular frequency in a Paul trap scales with the charge-to-mass ratio of the trapped ion. For our experimental parameters the values are 3.6 MHz, 4.8 MHz, and 7.2 MHz for He⁺, H₃⁺, and H₂⁺, respectively. In large ion crystals, space charge effects and the mechanical coupling between the ions shift the secular resonances from the single-particle values [69–71]. Nonetheless, we can clearly identify the three different species in the spectra. Since the measurement is nondestructive, we can repeat it and track the time evolution of the particle numbers. The orange trace in Fig. 10a was recorded 21 s after the blue trace. H₂⁺ ions can react with H₂ from the residual gas in the vacuum

chamber according to the exothermic chemical reaction $\text{H}_2^+ + \text{H}_2 \rightarrow \text{H}_3^+ + \text{H}$ [72]. In the orange trace, the H₂⁺ peak has vanished, while the height of the H₃⁺ peak has increased compared to the blue trace. Figure 10b shows the time evolution of the heights of both peaks. The clearly visible step indicates that the ion crystal originally contained a single H₂⁺ ion which then reacted to H₃⁺. The clear signature of a single H₂⁺ ion in the secular spectrum makes us confident that we can also detect the appearance of a single He²⁺ ion in a mixed Be⁺/He⁺ ion crystal.

5 Conclusion and outlook

The excitation dynamics of the 1S–2S transition in He⁺ depends on many parameters. These include the power of the XUV radiation that drives the transition and that can contribute to ionization from the 2S state, the focal size, the reduction of the carrier power due to residual phase noise [50], and perturbations of the ions by the trapping RF field [18]. Some of these contributions are difficult to estimate accurately. According to our rough estimate, a 60.8 nm frequency comb with an average power of 10 μW at the target should resonantly ionize a single He⁺ ion to He²⁺ with a reasonable rate of > 0.1 Hz. The output power of our 60.8 nm frequency comb setup needs to be increased a bit further by sending more power to the resonator for HHG, optimizing the focusing parameters for HHG, and operating the HHG with a He/Xe gas mixture. The spectral envelope of the 60.8-nm comb must be carefully tuned to maximize the overlap with the transition wavelength. We plan to accomplish this by monitoring the spectrum of the 60.8-nm comb with a calibrated spectrometer while tuning the spectrum of the infrared frequency comb. The expected signal linewidth is a few kHz, dominated by the decoherence due to ionization and quenching of the 2S state. The AC Stark shift due to the XUV radiation and residual infrared light may exceed a few kHz. This can be accounted for by repeating the measurement with different comb powers. Other systematic effects are expected to be insignificant to achieve our first goal of determining the transition frequency with a relative uncertainty of $\sim 1 \times 10^{-11}$ (100 kHz).

An interesting intermediate step is to use the 5th harmonic of the infrared frequency comb to excite the 2s–3d two-photon transition in Be⁺. The transition can be driven by radiation at a wavelength of 204.0 nm [73]. From the 3d state, the Be⁺ ions can decay via the 2p state to the 2s ²S_{1/2} ($F = 1$) dark state. This can be detected efficiently using electron shelving.

The resulting natural linewidth of $\Gamma = 2\pi \times 176$ MHz [74] is much larger than the mode spacing of 40 MHz such that the comb structure will not be resolved. The excitation rate is therefore independent of the comb detuning, and line broadening effects such as Doppler broadening are unimportant. Nevertheless, the excitation rate can be used as a signal to optimize the

alignment of the spectroscopy laser beam onto the ions. Furthermore, due to the nonlinear behavior of the two-photon excitation, the signal increases when the counterpropagating pulses overlap at the ion position. Therefore, it can also be used to adjust the pulse-to-pulse delay in the Mach–Zehnder interferometer.

Given the expected signal linewidth (a few kHz) and the uncertainty in the theoretical prediction of the transition frequency (~ 60 kHz, see Sect. 2), finding the 1S–2S spectroscopy signal will require measurements at a few hundred different frequency points. Pre-aligning the setup using the Be^+ two-photon signal is therefore essential for minimizing the number of other experimental parameters that have to be scanned.

Acknowledgements This project has received funding from the European Research Council (ERC) under the European Union’s Horizon 2020 research and innovation programme (Grant Agreement No. 742247) and the Deutsche Forschungsgemeinschaft (DFG, German Research Foundation)-Project No. KA 4645/1-2. T. W. Hänsch acknowledges support from the Max-Planck Foundation.

Author contributions

All authors contributed equally to this work.

Funding Information Open Access funding enabled and organized by Projekt DEAL.

Data Availability Statement This manuscript has no associated data or the data will not be deposited. [Authors’ comment: The datasets generated and/or analysed during the current study are available from the corresponding author on reasonable request.]

Open Access This article is licensed under a Creative Commons Attribution 4.0 International License, which permits use, sharing, adaptation, distribution and reproduction in any medium or format, as long as you give appropriate credit to the original author(s) and the source, provide a link to the Creative Commons licence, and indicate if changes were made. The images or other third party material in this article are included in the article’s Creative Commons licence, unless indicated otherwise in a credit line to the material. If material is not included in the article’s Creative Commons licence and your intended use is not permitted by statutory regulation or exceeds the permitted use, you will need to obtain permission directly from the copyright holder. To view a copy of this licence, visit <http://creativecommons.org/licenses/by/4.0/>.

References

1. P.J. Mohr, D.B. Newell, B.N. Taylor, CODATA recommended values of the fundamental physical constants: 2014. *Rev. Mod. Phys.* **88**(3), 035009 (2016). <https://doi.org/10.1103/revmodphys.88.035009>
2. E. Tiesinga, P.J. Mohr, D.B. Newell, B.N. Taylor, CODATA recommended values of the fundamental physical constants: 2018. *Rev. Mod. Phys.* **93**(2), 025010 (2021). <https://doi.org/10.1103/RevModPhys.93.025010>
3. U.D. Jentschura, M. Haas, Two-loop effects and current status of the $^4\text{He}^+$ Lamb shift. *Can. J. Phys.* **85**(5), 531–540 (2007). <https://doi.org/10.1139/p07-020>
4. V.A. Yerokhin, K. Pachucki, V. Patkóš, Theory of the Lamb shift in hydrogen and light hydrogen-like ions. *Ann. Phys.* **531**(5), 1800324 (2019). <https://doi.org/10.1002/andp.201800324>
5. S.G. Karshenboim, F.S. Pavone, F. Bassani, M. Inguscio, T.W. Hänsch (eds.): The hydrogen atom: precision physics of simple atomic systems. Lecture notes in physics, vol. 570. Springer, Berlin (2001)
6. D. Hanneke, S. Fogwell, G. Gabrielse, New measurement of the electron magnetic moment and the fine structure constant. *Phys. Rev. Lett.* **100**(12), 120801 (2008). <https://doi.org/10.1103/PhysRevLett.100.120801>
7. D. Hanneke, S. Fogwell Hoogerheide, G. Gabrielse, Cavity control of a single-electron quantum cyclotron: measuring the electron magnetic moment. *Phys. Rev. A* **83**(5), 052122 (2011). <https://doi.org/10.1103/PhysRevA.83.052122>
8. L. Morel, Z. Yao, P. Cladé, S. Guellati-Khélifa, Determination of the fine-structure constant with an accuracy of 81 parts per trillion. *Nature* **588**(7836), 61–65 (2020). <https://doi.org/10.1038/s41586-020-2964-7>
9. R.H. Parker, C. Yu, W. Zhong, B. Estey, H. Müller, Measurement of the fine-structure constant as a test of the Standard Model. *Science* **360**(6385), 191–195 (2018). <https://doi.org/10.1126/science.aap7706>
10. G. Gabrielse, S.E. Fayer, T.G. Myers, X. Fan, Towards an improved test of the standard model’s most precise prediction. *Atoms* **7**(2), 45 (2019). <https://doi.org/10.3390/atoms7020045>
11. T. Aoyama, T. Kinoshita, M. Nio, Theory of the anomalous magnetic moment of the electron. *Atoms* **7**(1), 28 (2019). <https://doi.org/10.3390/atoms7010028>
12. A. Matveev, C.G. Parthey, K. Predehl, J. Alnis, A. Beyer, R. Holzwarth, T. Udem, T. Wilken, N. Kolachevsky, M. Abgrall, D. Rovera, C. Salomon, P. Laurent, G. Grosche, O. Terra, T. Legero, H. Schnatz, S. Weyers, B. Altschul, T.W. Hänsch, Precision measurement of the hydrogen 1S–2S frequency via a 920-km fiber link. *Phys. Rev. Lett.* **110**(23), 230801 (2013). <https://doi.org/10.1103/physrevlett.110.230801>
13. R. Pohl, R. Gilman, G.A. Miller, K. Pachucki, Muonic hydrogen and the proton radius puzzle. *Annu. Rev. Nucl. Part. Sci.* **63**(1), 175–204 (2013). <https://doi.org/10.1146/annurev-nucl-102212-170627>
14. T. Udem, Quantum electrodynamics and the proton size. *Nat. Phys.* **14**(6), 632–632 (2018). <https://doi.org/10.1038/s41567-018-0166-0>
15. A.D. Brandt, S.F. Cooper, C. Rasoar, Z. Burkley, A. Matveev, D.C. Yost, Measurement of the $2S_{1/2}$ – $8D_{5/2}$ transition in hydrogen. *Phys. Rev. Lett.* **128**(2), 023001 (2022). <https://doi.org/10.1103/PhysRevLett.128.023001>
16. R.S. Van Dyck, S.L. Zafonte, S. Van Liew, D.B. Pinegar, P.B. Schwinberg, Ultraprecise atomic mass measurement of the α particle and ^4He . *Phys. Rev. Lett.* **92**(22),

- 220802 (2004). <https://doi.org/10.1103/PhysRevLett.92.220802>
17. F. Heiße, S. Rau, F. Köhler-Langes, W. Quint, G. Werth, S. Sturm, K. Blaum, High-precision mass spectrometer for light ions. *Phys. Rev. A* **100**(2), 022518 (2019). <https://doi.org/10.1103/PhysRevA.100.022518>
 18. M. Herrmann, M. Haas, U.D. Jentschura, F. Kottmann, D. Leibfried, G. Saathoff, C. Gohle, A. Ozawa, V. Batteiger, S. Knünz, N. Kolachevsky, H.A. Schüssler, T.W. Hänsch, T. Udem, Feasibility of coherent XUV spectroscopy on the 1S–2S transition in singly ionized helium. *Phys. Rev. A* **79**(5), 052505 (2009). <https://doi.org/10.1103/physreva.79.052505>
 19. U.D. Jentschura, Self-energy correction to the two-photon decay width in hydrogenlike atoms. *Phys. Rev. A* **69**(5), 052118 (2004). <https://doi.org/10.1103/physreva.69.052118>
 20. A. Czarnecki, R. Szafron, Light-by-light scattering in the Lamb shift and the bound electron g factor. *Phys. Rev. A* **94**(6), 060501 (2016). <https://doi.org/10.1103/PhysRevA.94.060501>
 21. S.G. Karshenboim, V.G. Ivanov, Higher-order logarithmic contributions to the Lamb shift in hydrogen, deuterium, and He⁺. *Phys. Rev. A* **98**(2), 022522 (2018). <https://doi.org/10.1103/PhysRevA.98.022522>
 22. S.G. Karshenboim, A. Ozawa, V.A. Shelyuto, R. Szafron, V.G. Ivanov, The lamb shift of the 1s state in hydrogen: two-loop and three-loop contributions. *Phys. Lett. B* **795**, 432–437 (2019). <https://doi.org/10.1016/j.physletb.2019.06.023>
 23. R. Szafron, E.Y. Korzinin, V.A. Shelyuto, V.G. Ivanov, S.G. Karshenboim, Virtual delbrück scattering and the lamb shift in light hydrogenlike atoms. *Phys. Rev. A* **100**(3), 032507 (2019). <https://doi.org/10.1103/PhysRevA.100.032507>
 24. S.G. Karshenboim, A. Ozawa, V.G. Ivanov, Higher-order logarithmic corrections and the two-loop self-energy of a 1s electron in hydrogen. *Phys. Rev. A* **100**(3), 032515 (2019). <https://doi.org/10.1103/PhysRevA.100.032515>
 25. S.G. Karshenboim, V.A. Shelyuto, Three-loop radiative corrections to the 1s lamb shift in hydrogen. *Phys. Rev. A* **100**(3), 032513 (2019). <https://doi.org/10.1103/PhysRevA.100.032513>
 26. V.A. Yerokhin, V.M. Shabaev, Nuclear recoil corrections to the lamb shift of hydrogen and light hydrogenlike ions. *Phys. Rev. A* **93**(6), 062514 (2016). <https://doi.org/10.1103/PhysRevA.93.062514>
 27. S. Laporta, High-precision calculation of the 4-loop QED contribution to the slope of the dirac form factor. *Phys. Lett. B* **800**, 135137 (2020). <https://doi.org/10.1016/j.physletb.2019.135137>
 28. S. Laporta, High-precision calculation of the 4-loop contribution to the electron g-2 in QED. *Phys. Lett. B* **772**, 232–238 (2017). <https://doi.org/10.1016/j.physletb.2017.06.056>
 29. T. Aoyama, M. Hayakawa, T. Kinoshita, M. Nio, Revised value of the eighth-order contribution to the electron g-2. *Phys. Rev. Lett.* **99**(11), 110406 (2007). <https://doi.org/10.1103/PhysRevLett.99.110406>
 30. P.A. Baikov, A. Maier, P. Marquard, The qed vacuum polarization function at four loops and the anomalous magnetic moment at five loops. *Nucl. Phys. B* **877**(3), 647–661 (2013). <https://doi.org/10.1016/j.nuclphysb.2013.10.020>
 31. J.J. Krauth, K. Schuhmann, M.A. Ahmed, F.D. Amaro, P. Amaro, F. Biraben, T.-L. Chen, D.S. Covita, A.J. Dax, M. Diepold, L.M.P. Fernandes, B. Franke, S. Galtier, A.L. Gouvea, J. Götzfried, T. Graf, T.W. Hänsch, J. Hartmann, M. Hildebrandt, P. Indelicato, L. Julien, K. Kirch, A. Knecht, Y.-W. Liu, J. Machado, C.M.B. Monteiro, F. Mulhauser, B. Naar, T. Nebel, F. Nez, J.M.F. dos Santos, J.P. Santos, C.I. Szabo, D. Taquu, J.F.C.A. Veloso, J. Vogelsang, A. Voss, B. Weichelt, R. Pohl, A. Antognini, F. Kottmann, Measuring the α -particle charge radius with muonic helium-4 ions. *Nature* **589**(7843), 527–531 (2021). <https://doi.org/10.1038/s41586-021-03183-1>
 32. I. Sick, Precise root-mean-square radius of ⁴He. *Phys. Rev. C* **77**(4), 041302 (2008). <https://doi.org/10.1103/PhysRevC.77.041302>
 33. A. Antognini, F. Hagelstein, V. Pascalutsa, The proton structure in and out of muonic hydrogen. *Annu. Rev. Nucl. Part. Sci.* **72**(1), 389–418 (2022). <https://doi.org/10.1146/annurev-nucl-101920-024709>
 34. K. Pachucki, A.M. Moro, Nuclear polarizability of helium isotopes in atomic transitions. *Phys. Rev. A* **75**(3), 032521 (2007). <https://doi.org/10.1103/PhysRevA.75.032521>
 35. Y.R. Sun, S.-M. Hu, Precision spectroscopy of atomic helium. *Natl. Sci. Rev.* **7**(12), 1818–1827 (2020). <https://doi.org/10.1093/nsr/nwaa216>
 36. K. Pachucki, V. Patkóš, V.A. Yerokhin, Testing fundamental interactions on the helium atom. *Phys. Rev. A* **95**(6), 062510 (2017). <https://doi.org/10.1103/PhysRevA.95.062510>
 37. R.J. Rengelink, Y. van der Werf, R.P.M.J.W. Notermans, R. Jannin, K.S.E. Eikema, M.D. Hoogerland, W. Vassen, Precision spectroscopy of helium in a magic wavelength optical dipole trap. *Nat. Phys.* **14**(11), 1132–1137 (2018). <https://doi.org/10.1038/s41567-018-0242-5>
 38. X. Zheng, Y.R. Sun, J.-J. Chen, W. Jiang, K. Pachucki, S.-M. Hu, Measurement of the frequency of the 2³S–2³P transition of ⁴He. *Phys. Rev. Lett.* **119**(26), 263002 (2017). <https://doi.org/10.1103/PhysRevLett.119.263002>
 39. P. Cancio Pastor, L. Consolino, G. Giusfredi, P. De Natale, M. Inguscio, V.A. Yerokhin, K. Pachucki, Frequency metrology of helium around 1083 nm and determination of the nuclear charge radius. *Phys. Rev. Lett.* **108**(14), 143001 (2012). <https://doi.org/10.1103/PhysRevLett.108.143001>
 40. R. van Rooij, J.S. Borbely, J. Simonet, M.D. Hoogerland, K.S.E. Eikema, R.A. Rozendaal, W. Vassen, Frequency metrology in quantum degenerate helium: direct measurement of the 2³S₁ → 2¹S₀ transition. *Science* **333**(6039), 196–198 (2011). <https://doi.org/10.1126/science.1205163>
 41. D. Shiner, R. Dixon, V. Vedantham, Three-nucleon charge radius: a precise laser determination using ³He. *Phys. Rev. Lett.* **74**(18), 3553–3556 (1995). <https://doi.org/10.1103/PhysRevLett.74.3553>
 42. P. Russbueldt, D. Hoffmann, M. Höfer, J. Löhning, J. Luttmann, A. Meissner, J. Weitenberg, M. Traub, T. Sartorius, D. Esser, R. Wester, P. Loosen, R. Poprawe,

- Innoslab amplifiers. *IEEE J. Sel. Top. Quantum Electron.* **21**(1), 447–463 (2015). <https://doi.org/10.1109/JSTQE.2014.2333234>
43. J. Weitenberg, A. Vernaleken, J. Schulte, A. Ozawa, T. Sartorius, V. Pervak, H.-D. Hoffmann, T. Udem, P. Russbldt, T.W. Hnsch, (2017). Multi-pass-cell-based nonlinear pulse compression to 115 fs at 7.5 μ J pulse energy and 300 W average power. *Opt. Express*, **25**(17), 20502–20510. <https://doi.org/10.1364/OE.25.020502>
 44. J. Schulte, T. Sartorius, J. Weitenberg, A. Vernaleken, P. Russbldt, Nonlinear pulse compression in a multi-pass cell. *Opt. Lett.* **41**(19), 4511–4514 (2016). <https://doi.org/10.1364/OL.41.004511>
 45. C. Gohle, T. Udem, M. Herrmann, J. Rauschenberger, R. Holzwarth, H.A. Schuessler, F. Krausz, T.W. Hnsch, A frequency comb in the extreme ultraviolet. *Nature* **436**(7048), 234–237 (2005). <https://doi.org/10.1038/nature03851>
 46. R.J. Jones, K.D. Moll, M.J. Thorpe, J. Ye, Phase-coherent frequency combs in the vacuum ultraviolet via high-harmonic generation inside a femtosecond enhancement cavity. *Phys. Rev. Lett.* **94**(19), 193201 (2005). <https://doi.org/10.1103/physrevlett.94.193201>
 47. A. Ozawa, J. Rauschenberger, C. Gohle, M. Herrmann, D.R. Walker, V. Pervak, A. Fernandez, R. Graf, A. Apolonski, R. Holzwarth, F. Krausz, T.W. Hnsch, T. Udem, High harmonic frequency combs for high resolution spectroscopy. *Phys. Rev. Lett.* **100**(25), 253901 (2008). <https://doi.org/10.1103/physrevlett.100.253901>
 48. I. Pupeza, C. Zhang, M. Hgner, J. Ye, Extreme-ultraviolet frequency combs for precision metrology and attosecond science. *Nat. Photonics* **15**(3), 175–186 (2021). <https://doi.org/10.1038/s41566-020-00741-3>
 49. C. Benko, T.K. Allison, A. Cingz, L. Hua, F. Labaye, D.C. Yost, J. Ye, Extreme ultraviolet radiation with coherence time greater than 1 s. *Nat. Photonics* **8**(7), 530–536 (2014). <https://doi.org/10.1038/nphoton.2014.132>
 50. F. Schmid, J. Weitenberg, T.W. Hnsch, T. Udem, A. Ozawa, Simple phase noise measurement scheme for cavity-stabilized laser systems. *Opt. Lett.* **44**(11), 2709 (2019). <https://doi.org/10.1364/ol.44.002709>
 51. J. Hald, V. Ruseva, Efficient suppression of diode-laser phase noise by optical filtering. *J. Opt. Soc. Am. B* **22**(11), 2338 (2005). <https://doi.org/10.1364/josab.22.002338>
 52. R.W.P. Drever, J.L. Hall, F.V. Kowalski, J. Hough, G.M. Ford, A.J. Munley, H. Ward, Laser phase and frequency stabilization using an optical resonator. *Appl. Phys. B* **31**(2), 97–105 (1983). <https://doi.org/10.1007/bf00702605>
 53. D. Esser, J. Weitenberg, W. Brring, I. Pupeza, S. Holzberger, H.-D. Hoffmann, Laser-manufactured mirrors for geometrical output coupling of intracavity-generated high harmonics. *Opt. Express* **21**(22), 26797–26805 (2013). <https://doi.org/10.1364/OE.21.026797>
 54. C. Zhang, S.B. Schoun, C.M. Heyl, G. Porat, M.B. Gaarde, J. Ye, Noncollinear enhancement cavity for record-high out-coupling efficiency of an extreme-UV frequency comb. *Phys. Rev. Lett.* **125**(9), 093902 (2020). <https://doi.org/10.1103/PhysRevLett.125.093902>
 55. T.K. Allison, A. Cingz, D.C. Yost, J. Ye, Extreme nonlinear optics in a femtosecond enhancement cavity. *Phys. Rev. Lett.* **107**(18), 183903 (2011). <https://doi.org/10.1103/PhysRevLett.107.183903>
 56. K.D. Moll, R.J. Jones, J. Ye, Output coupling methods for cavity-based high-harmonic generation. *Opt. Express* **14**(18), 8189–8197 (2006). <https://doi.org/10.1364/OE.14.008189>
 57. J. Weitenberg, S. Wissenberg, J. Moreno, T. Rozibakieva, F. Schmid, H.-D. Hoffmann, T. Udem, T.W. Hnsch, A. Ozawa, Non-collinear enhancement resonator with intrinsic pulse synchronization and alignment employing wedge mirrors (manuscript in preparation, 2023)
 58. L. Hornekr, N. Kjrgaard, A.M. Thommesen, M. Drewsen, Structural properties of two-component coulomb crystals in linear Paul traps. *Phys. Rev. Lett.* **86**(10), 1994–1997 (2001). <https://doi.org/10.1103/physrevlett.86.1994>
 59. F. Schmid, J. Weitenberg, J. Moreno, T.W. Hnsch, T. Udem, A. Ozawa, Number-resolved detection of dark ions in coulomb crystals. *Phys. Rev. A* **106**(4), 041101 (2022). <https://doi.org/10.1103/PhysRevA.106.L041101>
 60. W.W. Macalpine, R.O. Schildknecht, Coaxial resonators with helical inner conductor. *Proc. IRE* **47**(12), 2099–2105 (1959). <https://doi.org/10.1109/jrproc.1959.287128>
 61. H.-Y. Lo, J. Alonso, D. Kienzler, B.C. Keitch, L.E. de Clercq, V. Negnevitsky, J.P. Home, All-solid-state continuous-wave laser systems for ionization, cooling and quantum state manipulation of beryllium ions. *Appl. Phys. B* **114**(1–2), 17–25 (2013). <https://doi.org/10.1007/s00340-013-5605-0>
 62. J.R. Fuhr, W.L. Wiese, Tables of atomic transition probabilities for beryllium and boron. *J. Phys. Chem. Ref. Data* **39**(1), 013101 (2010). <https://doi.org/10.1063/1.3286088>
 63. A.C. Wilson, C. Ospelkaus, A.P. VanDevender, J.A. Mlynek, K.R. Brown, D. Leibfried, D.J. Wineland, A 750-mW, continuous-wave, solid-state laser source at 313 nm for cooling and manipulating trapped $^9\text{Be}^+$ ions. *Appl. Phys. B* **105**(4), 741–748 (2011). <https://doi.org/10.1007/s00340-011-4771-1>
 64. D.J. Wineland, J.J. Bollinger, W.M. Itano, Laser-fluorescence mass spectroscopy. *Phys. Rev. Lett.* **50**(9), 628–631 (1983). <https://doi.org/10.1103/physrevlett.50.628>
 65. N. Shiga, W.M. Itano, J.J. Bollinger, Diamagnetic correction to the $^9\text{Be}^+$ ground-state hyperfine constant. *Phys. Rev. A* **84**(1), 012510 (2011). <https://doi.org/10.1103/physreva.84.012510>
 66. G. Porat, C.M. Heyl, S.B. Schoun, C. Benko, N. Drre, K.L. Corwin, J. Ye, Phase-matched extreme-ultraviolet frequency-comb generation. *Nat. Photonics* **12**, 387–391 (2018). <https://doi.org/10.1038/s41566-018-0199-z>
 67. O. Pronin, V. Pervak, E. Fill, J. Rauschenberger, F. Krausz, A. Apolonski, Ultrabroadband efficient intracavity XUV output coupler. *Opt. Express* **19**(11), 10232–10240 (2011). <https://doi.org/10.1364/OE.19.010232>
 68. Y. Colombe, D.H. Slichter, A.C. Wilson, D. Leibfried, D.J. Wineland, Single-mode optical fiber for high-

- power, low-loss UV transmission. *Opt. Express* **22**(16), 19783 (2014). <https://doi.org/10.1364/oe.22.019783>
69. B. Roth, P. Blythe, S. Schiller, Motional resonance coupling in cold multispecies coulomb crystals. *Phys. Rev. A* **75**(2), 023402 (2007). <https://doi.org/10.1103/physreva.75.023402>
70. C.B. Zhang, D. Offenber, B. Roth, M.A. Wilson, S. Schiller, Molecular-dynamics simulations of cold single-species and multispecies ion ensembles in a linear paul trap. *Phys. Rev. A* **76**(1), 012719 (2007). <https://doi.org/10.1103/physreva.76.012719>
71. B.-M. Ann, F. Schmid, J. Krause, T.W. Hänsch, T. Udem, A. Ozawa, Motional resonances of three-dimensional dual-species coulomb crystals. *J. Phys. B At. Mol. Opt. Phys.* **52**(3), 035002 (2019). <https://doi.org/10.1088/1361-6455/aaf5ea>
72. M.T. Bowers, D.D. Elleman, J. King, Analysis of the ion-molecule reactions in gaseous H₂, D₂, and HD by ion cyclotron resonance techniques. *J. Chem. Phys.* **50**(11), 4787–4804 (1969). <https://doi.org/10.1063/1.1670971>
73. A.E. Kramida, Critical compilation of wavelengths and energy levels of singly ionized beryllium (Be II). *Phys. Scr.* **72**(4), 309–319 (2005). <https://doi.org/10.1238/physica.regular.072a00309>
74. C. Froese Fischer, M. Saporov, G. Gaigalas, M. Godefroid, Breit-pauli energies, transition probabilities, and lifetimes for 2s, 2p, 3s, 3p, 3d, 4s ²L levels of the lithium sequence, Z = 3–8. *At. Data Nucl. Data Tables* **70**(1), 119–134 (1998). <https://doi.org/10.1006/adnd.1998.0788>